



Shape analysis of a rotating axisymmetric drop in gravitational field: Comparison of numerical schemes for real-time data processing



Krassimir D. Danov^{a,*}, Stefka N. Dimova^b, Tihomir B. Ivanov^{b,c}, Javor K. Novev^a

^a Department of Chemical and Pharmaceutical Engineering, Faculty of Chemistry and Pharmacy, Sofia University, 1164 Sofia, Bulgaria

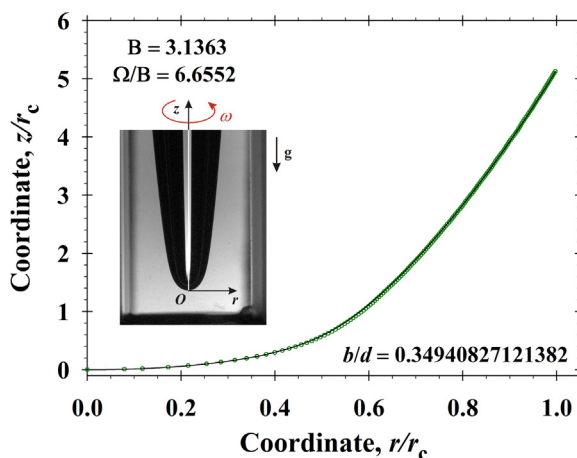
^b Department of Numerical Methods and Algorithms, Faculty of Mathematics and Informatics, Sofia University, 1164 Sofia, Bulgaria

^c Department of Mathematical Modeling and Numerical Analysis, Institute of Mathematics and Informatics, 1113 Sofia, Bulgaria

HIGHLIGHTS

- Axisymmetric drop/bubble subjected to centrifugal and gravitational accelerations.
- Comparison of numerical schemes for data processing.
- Effective real-time algorithms for determination of surface tension.

GRAPHICAL ABSTRACT



ARTICLE INFO

Article history:

Received 15 September 2015

Received in revised form 16 October 2015

Accepted 18 October 2015

Available online 21 October 2015

Keywords:

Young–Laplace equation of capillarity
Drops in rotational and gravitational fields
Runge–Kutta methods
Taylor, Adams–Bashforth, Adams–Moulton, predictor–corrector methods
Stability and computational time
Axisymmetric drop shape analysis

ABSTRACT

The classical axisymmetric drop shape analysis (ADSA) method is used to measure the surface tensions and contact angles from the best fit of drop images with the Young–Laplace equation of capillarity. To produce well deformed drops needed for better precision, one applies rotation with a sufficiently high angular velocity in addition to the gravitational field. Without rotation, the conventional fourth-order Runge–Kutta and second-order Taylor methods are suitable for obtaining the numerical solution of the Young–Laplace equation required for ADSA, but they are slow for the case of a rotating drop in gravitational field. The real-time data processing of images of rotating drops requires relatively simple, high-precision, and stable numerical methods working with a well-defined fixed computational time. This study aims to develop the sixth-order Taylor method (T6) for the specific problem and to compare its accuracy, stability, and computational time with the available classes of Runge–Kutta (fifth-, sixth-, tenth-orders, and second-order 3-stage method with step control), Adams–Bashforth (sixth- and seventh-orders), and predictor–corrector methods based on the seventh-order Adams–Moulton approach (PC76 and PC77). The ranges of stability of these methods under variation of the parameters characterizing the capillary profiles are obtained and their computational times, tested on the experimental data

* Corresponding author. Fax: +359 29625643.

E-mail address: kd@lcpe.uni-sofia.bg (K.D. Danov).

for rotating drops in gravitational field, are compared. From the viewpoint of real-time data processing, the most appropriate methods are T6, PC76, and PC77 because of their high precision, good stability, and sufficiently short predictable computational times.

© 2015 Elsevier B.V. All rights reserved.

1. Introduction

The first attempt to test the Young–Laplace equation of capillarity, made by Bashforth and Adams [1], compared the experimental and theoretical shapes of liquid drops. It was based on the axisymmetric solution of the system of three differential equations for the drop radial, r , and vertical, z , coordinates and the meniscus running slope angle, θ , as functions of the drop arc length, s . The calculated parameters for sessile drops were summarized in tables [1]; for pendant drops, they were published later on by Andreas et al. [2] and Fordham [3], who determined the interfacial tension, σ , from the specific meniscus dimensions. These tables were the tools for calculations of σ and contact angles, α_c , from experimental data for a long time, see Ref. [4] for a detailed review. After the pioneering work of Rotenberg et al. [5] for the calculation of surface tension (Fig. 1a) and contact angles (Fig. 1b) from the shapes of axisymmetric fluid interfaces in gravitational field, g , and the advent of computer image analysis, the pendant drop method has become fully automated. The axisymmetric drop shape analysis (ADSA) method has found a wide range of applications for the measurements of static and dynamic surface tension, interfacial rheology [6–9], three-phase contact angles [10–12], the mechanism of oil-drop detachment [13,14], etc. The accuracy of the measurements and the role of image analysis have been investigated in Refs. [7,15]. In essence, ADSA works by matching a theoretical profile of the drop to the extracted experimental profile, taking the surface tension, σ , and the capillary pressure at the drop apex, $2\sigma/b$ with b being the radius of curvature at the apex, as adjustable parameters.

The spinning drop method is one of the most useful approaches for measuring low interfacial tensions. When a drop/bubble (phase 1 of density ρ_1) is placed in a liquid of higher density (phase 2 of density $\rho_2 > \rho_1$), contained in a rotating horizontal tube, it becomes elongated along the axis of revolution, Oz (Fig. 1c). The effect of gravity can be neglected for small drops, as done by Vonnegut [16], who developed an approximate theory and proposed a method for measuring interfacial tensions. The exact solution of the problem for $g = 0$ in terms of elliptic integrals of the first and second kind was published in Refs. [17,18], where an excellent agreement between theory and experiment was achieved. An important parameter of the investigated systems is the relaxation time, that is, the time required for attaining the equilibrium drop shape [18,19]. One of the general problems in the application of spinning drop tensiometry to very low interfacial tensions is that the drop becomes unstable—the Rayleigh instability leads to drop breakup in the centrifugal field [20].

To avoid the instability of drops/bubbles in the conventional spinning drop method, Aronson and Princen [21] suggested the use of a vertical configuration (Fig. 1d), in which the gravitational field suppresses the destabilizing effect of the rotation when the outer fluid is heavier. The authors calculated the shape of a meniscus in a rotating vertical tube under the action of gravity, tabulated the obtained numerical results for different values of the three-phase contact angles, and performed experiments to show that this approach is applicable for interfacial tension measurements. Later, this model was applied to calculate numerically the shape of a sessile droplet on a rotating solid substrate [22]. This technique has no automated version because of the numerical difficulties

of calculating the theoretical profiles (see Section 5) needed for ADSA.

Two algorithms for numerically solving the Young–Laplace equation are used in the available equipment: (i) the second-order Taylor method [5]; (ii) the classical fourth-order Runge–Kutta method with a built-in step size adjustment [15,21]. The aim of our study is to develop the sixth-order Taylor method (T6) for the specific problem and to compare its accuracy, stability, and computational time with the available classes of Runge–Kutta, Adams–Bashforth, and predictor–corrector methods.

A historical review of Runge–Kutta methods was made by Butcher [23]. After the publications of Butcher [24–26] and Fehlberg [27], numerous realizations of the method were reported in the literature. Below, we compare our algorithm with the classical fourth-order, Cash and Karp fifth-order [28], Verner sixth-order [29], and Feagin tenth-order [30] Runge–Kutta methods. The Young–Laplace equation of capillarity (see Section 2) is a second-order nonlinear differential equation for $z(r)$, to which the original Simos approach [31,32] is not applicable because z can have more than one value for a given radial distance r (see Fig. 1a).

The Adams–Bashforth (AB) method was originally developed to solve numerically the Young–Laplace equation [1]. The formulas for the coefficients of this method generalized to arbitrary order can be found in the literature, e.g., in Ref. [33]. Often, a combination of the explicit AB method and the implicit Adams–Moulton (AM) method [34] is used as a predictor–corrector (PC) method. Both the AB and the PC methods are fast because for each step the right-hand side of equations is calculated only once (for AB) or twice (for PC).

In the presence of surface-active substances, the interfacial tension, σ , changes with time and drop area A . Even at a constant drop volume, V , because of the decreasing of σ , the drop area increases. For many practical and scientific applications the measurements must be performed at constant values of V , A , or σ [9,35]. To implement such a feedback, the instantaneous values of the volume, area, and surface tension must be calculated in real time. While the volume and area can be calculated from the images with a relatively good precision using geometrical approaches, the values of the surface tension are determined from the numerical solution of the respective Young–Laplace equation. Thus one needs a numerical method for solving the specific problem, which satisfies the following requirements: (i) relative simplicity; (ii) well-defined fixed computational time for one profile; (iii) good accuracy; (iv) stability under change of the adjustable parameters b and σ .

2. Mathematical formulation of the problem

Let us consider a drop/bubble subjected to centrifugal and gravitational accelerations that are perpendicular to each other (Fig. 1). The density of the inner phase is ρ_1 and that of the outer phase is ρ_2 —here $\rho_1 \neq \rho_2$ and the inner phase can be lighter or heavier than the outer one. The problem is axisymmetric and it can be solved in cylindrical coordinates, r and z . The origin of the coordinate system is located at the drop apex (Fig. 1). The pressures inside and outside the boundary are p_1 and p_2 , respectively. Both of them contain hydrostatic and centrifugal contributions:

$$p_k = p_{k,0} + \rho_k \frac{\omega^2 r^2}{2} + \rho_k z \mathbf{g} \cdot \mathbf{e}_z \quad (k = 1, 2) \quad (2.1)$$

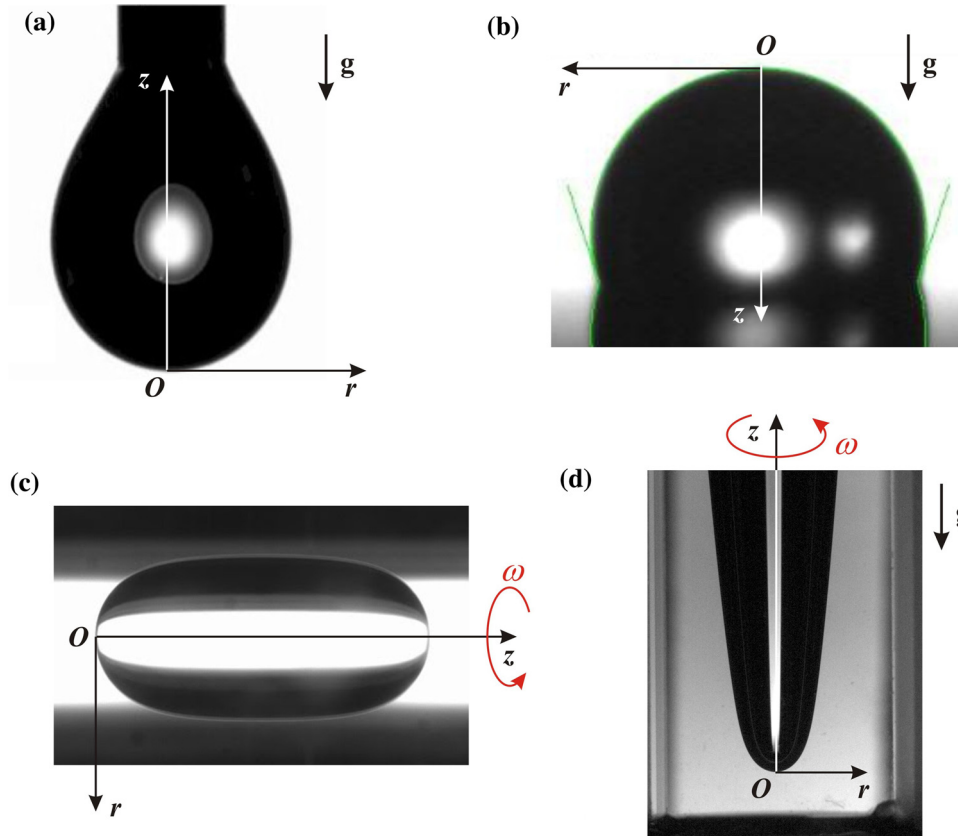


Fig. 1. Axisymmetric capillary shapes in typical experimental equipment: (a) pendant drop; (b) sessile drop; (c) rotating small drop (spinning drop method); (d) rotating drop in gravitational field—the outer fluid is heavier.

where \mathbf{g} is the acceleration due to gravity; \mathbf{e}_z is the unit basis vector along the axis of revolution; ω is the angular velocity; $p_{k,0}$ is the pressure at the drop apex in the k th phase.

The pressure difference $p_1 - p_2$ is balanced by the capillary pressure due to the curvature of the meniscus (Young–Laplace equation) [21,36]:

$$2H\sigma = p_1 - p_2 \quad (2.2)$$

where H is the mean curvature of the capillary surface. At the drop apex ($r=0, z=0$), $H = 1/b$ and then Eq. (2.2) acquires the form, $p_{1,0} - p_{2,0} = 2\sigma/b$. Thus, from Eqs. (2.1) and (2.2) one obtains:

$$2H\sigma = \frac{2\sigma}{b} + (\rho_1 - \rho_2)\frac{\omega^2 r^2}{2} + (\rho_1 - \rho_2)z\mathbf{g} \cdot \mathbf{e}_z \quad (2.3)$$

To distinguish the different possible cases, we rewrite Eq. (2.3) in the following equivalent form:

$$2H = \frac{2}{b} - \epsilon_\omega \frac{\Delta\rho}{2\sigma} \omega^2 r^2 + \epsilon_g \frac{\Delta\rho}{\sigma} gz \quad \text{and} \quad \Delta\rho \equiv |\rho_1 - \rho_2| \quad (2.4)$$

where: $\epsilon_g = 0$ if the effect of gravity is negligible; $\epsilon_g = -1$ when the gravity field elongates the drop/bubble profile (Fig. 1a), whereas $\epsilon_g = 1$ in the opposite case (Fig. 1b); $\epsilon_\omega = 0$ without rotation; $\epsilon_\omega = 1$ for a typical spinning drop configuration ($\rho_2 > \rho_1$), see Fig. 1c and d; $\epsilon_\omega = -1$ for $\rho_2 < \rho_1$, when without gravity the centrifugal field leads to the formation of a dimple (“red blood cell”) as the speed of rotation increases. Finally, introducing the running slope angle, θ , we can express the mean curvature in terms of the slope angle and its derivative, obtaining the following equation for the interfacial profile [8]:

$$\frac{d\sin\theta}{dr} + \frac{\sin\theta}{r} = \frac{2}{b} - \epsilon_\omega \frac{\Delta\rho}{2\sigma} \omega^2 r^2 + \epsilon_g \frac{\Delta\rho}{\sigma} gz \quad (2.5)$$

see Refs. [21,22]. Eq. (2.5) reduces to the problem considered by Princen et al. [17] for $g=0$, whereas for $\omega=0$ it becomes identical to the basic equation of the conventional ADSA.

Note that Eq. (2.5) can also be presented in the following form

$$d(r\sin\theta) = \frac{2r}{b} dr - \epsilon_\omega \frac{\Delta\rho}{2\sigma} \omega^2 r^3 dr + \epsilon_g \frac{\Delta\rho}{\sigma} gz r dr \quad (2.6)$$

that is,

$$\epsilon_g \Delta\rho g r^2 dz = d\left(\frac{2\sigma}{b} r^2 - \epsilon_\omega \frac{\Delta\rho}{4} \omega^2 r^4 + \epsilon_g \Delta\rho g z r^2 - 2\sigma r \sin\theta\right) \quad (2.7)$$

One multiplies Eq. (2.7) by π and integrates the obtained result from the apex to a given vertical distance z to derive an exact expression for the volume:

$$\epsilon_g \Delta\rho g V = \left(\frac{2\sigma}{b} - \epsilon_\omega \frac{\Delta\rho}{4} \omega^2 r^2 + \epsilon_g \Delta\rho g z\right) \pi r^2 - \sigma(2\pi r \sin\theta) \quad (2.8)$$

In the absence of gravity ($g=0$), the first integral, Eq. (2.8), cannot be used for calculation of the volume.

It is convenient to express the Young–Laplace equation, Eq. (2.5), in terms of the arc length, s , along the generatrix of the drop profile [37]:

$$\frac{dr}{ds} = \cos\theta, \quad \frac{dz}{ds} = \sin\theta \quad (2.9)$$

$$\frac{d\theta}{ds} = \frac{2}{b} - \frac{\sin\theta}{r} - \epsilon_\omega \frac{\Delta\rho}{2\sigma} \omega^2 r^2 + \epsilon_g \frac{\Delta\rho}{\sigma} gz \quad (2.10)$$

The system of differential equations, Eqs. (2.9) and (2.10), is solved numerically using the following initial conditions at the drop apex (at $s=0$):

$$r(0) = 0, \quad z(0) = 0, \quad \theta(0) = 0 \quad (2.11)$$

If the values of the area, A , and the volume, V , are needed, then we simply extend the system of equations, Eqs. (2.9) and (2.10), and the initial conditions, Eq. (2.11), with the following relationships:

$$\frac{dA}{ds} = 2\pi r \quad \text{and} \quad A(0) = 0 \quad (2.12)$$

$$\frac{dV}{ds} = \pi r^2 \sin\theta \quad \text{and} \quad V(0) = 0 \quad (2.13)$$

3. Initial value problem and numerical methods

For the numerical calculations, we scale all geometrical parameters with a characteristic distance d . For the mathematical analysis [17,36], usually the scaling is performed with the radius of curvature at the apex, that is with $d = b$. This is not convenient for the data processing of experimental images because the natural adjustable parameters are b and σ . In the case of drops/bubbles attached to a capillary (Fig. 1a and d), the typical scaling parameter, d , is the radius of the capillary. In the case of a spinning drop (Fig. 1c), d is the radius of the spherical drop with the same volume as the deformed one. For measurements of the contact angle, d characterizes the radius of the three-phase contact line or the drop height. We introduce:

$$y_1 \equiv \frac{r}{d}, y_2 \equiv \frac{z}{d}, y_3 \equiv \theta, y_4 \equiv \frac{A}{2\pi d^2}, y_5 \equiv \frac{V}{\pi d^3} \quad (3.1)$$

and the dimensionless arc length, $t \equiv s/d$. The initial value problem for $y(t) = (y_1, y_2, \dots, y_5)^T$, described in Section 2, is reduced to the following dimensionless system of differential equations:

$$\frac{dy}{dt} = f(y) \quad \text{and} \quad f = (f_1, f_2, \dots, f_5)^T \quad (3.2)$$

$$f_1 \equiv \cos y_3, f_2 \equiv \sin y_3, f_4 \equiv y_1, f_5 = y_1^2 \sin y_3 \quad (3.3)$$

$$f_3 \equiv 2 \frac{d}{b} - \frac{\sin y_3}{y_1} - \epsilon_\omega \Omega y_1^2 + \epsilon_g B y_2 \quad (3.4)$$

with zero initial conditions, see Eqs. (2.11)–(2.13). In Eq. (3.4) $B \equiv \Delta \rho g d^2 / \sigma$ is the Bond number (originally introduced by Loránd Eötvös and also called the Eötvös number); $\Omega \equiv \Delta \rho \omega^2 d^3 / (2\sigma)$ is the dimensionless parameter controlling the shapes of the spinning drop [17]—this parameter is also related to the rotational Froude number, $Fr \equiv \Omega / B = \omega^2 d / (2g)$ [18], which characterizes the ratio of the centripetal and gravitational accelerations.

Because of the restrictions of real-time data processing (see Section 1) the implicit Runge–Kutta methods are not convenient. Moreover, it is important for the numerical algorithm to be defined at a given constant step h in order to have a fixed time for the computations of the theoretical capillary profiles.

3.1. Explicit Runge–Kutta methods

Below, the initial value problem, Eqs. (3.2)–(3.4), is solved numerically using four different versions of the explicit Runge–Kutta method. For brevity, the classical fourth-order scheme will be hereafter referred to as RK4. We tested different fifth-, sixth-, and tenth-order Butcher tableaux and found that for our problem the Cash and Karp fifth-order (RK5), Verner sixth-order (RK6), and Feagin tenth-order (RK10) schemes are the most appropriate. The Butcher tableaux for these methods are given in Refs. [28–30], respectively. Note that the right-hand side of Eq. (3.4) has a singularity at $y_1 \rightarrow 0$. At the initial point Eq. (3.4) acquires the following asymptotic form:

$$f_3 = \frac{d}{b} \quad \text{at} \quad t \rightarrow 0 \quad (3.5)$$

which is used as a definition of the initial value of f_3 , see Eqs. (3.4) and (A.20)–(A.22) in Appendix A.

3.2. Second-order 3-stage explicit Runge–Kutta method with step control

From the classes of explicit Runge–Kutta methods with step control, we tested below the second-order 3-stage method (RK23) because of the small number of calculations of the right-hand side of the studied system and the extended region of stability [38]. The formulas for the solution at the moment $t+h$ read [39]:

$$y(t+h) = y_0 + \frac{1}{4}k_1 + \frac{15}{32}k_2 + \frac{9}{32}k_3 \quad \text{and} \quad y_0 \equiv y(t) \quad (3.6)$$

$$k_1 = hf(y_0), k_2 = hf(y_0 + \frac{2}{3}k_1), k_3 = hf(y_0 + \frac{1}{3}k_1 + \frac{1}{3}k_2) \quad (3.7)$$

where y is the vector of the solution and f is the vector of the right-hand side of the studied system. The step, h , is chosen in order to obey the following two conditions [39]:

i) for a given accuracy, ϵ , to have

$$\max_{1 \leq j \leq 5} \frac{|(k_2 - k_1)_j|}{|y_{0,j}| + \tau} \leq 6.4\epsilon \quad (3.8)$$

where τ is a tolerance used to control the relative error for $|y_{0,j}| \geq \tau$ and the absolute error for $|y_{0,j}| < \tau$ [39];

ii) the stability criterion,

$$\max_{1 \leq j \leq 5} \frac{|(k_3 - k_2)_j|}{|(k_2 - k_1)_j|} \leq 2 \quad (3.9)$$

to be fulfilled. The step control is performed for each value of t . In our case the inequality, Eq. (3.9), can always be satisfied by choosing a sufficiently small step h .

3.3. Explicit Taylor method

Because of the explicit forms of the right-hand sides of Eqs. (3.2)–(3.4), the Taylor method of arbitrary order n can be applied, that is:

$$y(t+h) = y_0 + \sum_{j=1}^n y^{(j)} \frac{h^j}{j!} + O(h^{n+1}) \quad \text{and} \quad y^{(j)} \equiv \frac{d^j y}{dt^j}(t) \quad (3.10)$$

where $j = 1, 2, \dots, n$. The obtained expressions for the derivatives, $y^{(j)}$ ($j \leq 6$), are listed in Appendix A. In the case without rotation and $n = 2$, the Taylor method is reported in Refs. [5,40,41].

3.4. AB, AM and PC methods

The numerical formulas for the explicit sixth- and seventh-order AB methods are based on the following expressions:

$$y_1 = y_0 + \frac{4277}{1440}hf(y_0) - \frac{2641}{480}hf(y_{-1}) + \frac{4991}{720}hf(y_{-2}) - \frac{3649}{720}hf(y_{-3}) + \frac{959}{480}hf(y_{-4}) - \frac{95}{288}hf(y_{-5}) + \frac{19087}{60480}y^{(7)}(t)h^7 + o(h^7) \quad (3.11)$$

$$y_1 = y_0 + \frac{198721}{60480}hf(y_0) - \frac{18637}{2520}hf(y_{-1}) + \frac{235183}{20160}hf(y_{-2}) - \frac{10754}{945}hf(y_{-3}) + \frac{135713}{20160}hf(y_{-4}) - \frac{5603}{2520}hf(y_{-5}) + \frac{19087}{60480}hf(y_{-6}) + \frac{5257}{17280}y^{(8)}(t)h^8 + o(h^8) \quad (3.12)$$

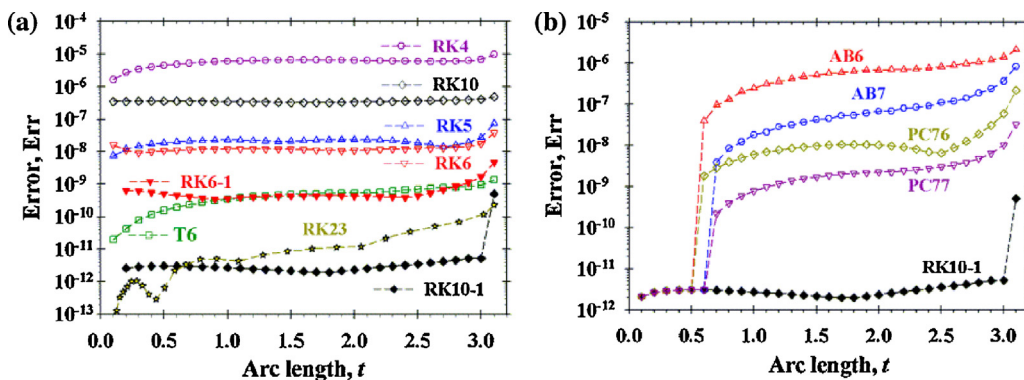


Fig. 2. Comparison of the errors of different numerical schemes for spherical shape: (a) Taylor and Runge–Kutta methods; (b) RK10-1, Adams–Bashforth and predictor–corrector methods. For all numerical methods $h = 0.1$ except of RK23 (see the text).

where $y_{-k} \equiv y(t - kh)$ ($k = -1, 0, 1, 2, \dots, 6$). Eq. (3.11) defines the sixth-order AB method (AB6) and Eq. (3.12) – the seventh-order AB method (AB7), respectively. The implicit seventh-order AM method uses the expansion:

$$\begin{aligned}
 y_1 = y_0 &+ \frac{19087}{60480} hf(y_1) + \frac{2713}{2520} hf(y_0) - \frac{15487}{20160} hf(y_{-1}) \\
 &+ \frac{586}{945} hf(y_{-2}) - \frac{6737}{20160} hf(y_{-3}) + \frac{263}{2520} hf(y_{-4}) \\
 &- \frac{863}{60480} hf(y_{-5}) - \frac{275}{24192} y^{(8)}(t)h^8 + o(h^8) \quad (3.13)
 \end{aligned}$$

It is important to note that the absolute value of the ratio between the last terms in Eqs. (3.13) and (3.12) is equal to $1375/36799 \approx 0.037$, so that Eq. (3.13) is about 27 times more precise than Eq. (3.12).

We used the expansion of the left- and right-hand sides of Eqs. (3.11)–(3.13) in series with respect to h and proved the validity of these formulas.

The idea of the PC methods is to replace $f(y_1)$ in Eq. (3.13) by $f(y_p)$, where the predicted value, y_p , is calculated from the explicit AB method. Thus, one obtains:

$$f(y_1) = f(y_p) + \sum_{j=1}^5 \frac{\partial f}{\partial y_j} \Big|_{y=y_p} (y_1 - y_p)_j + \dots \quad (3.14)$$

For example, if y_p is calculated from the AB6 method, see Eq. (3.11), then one derives:

$$f(y_1) = f(y_p) + \frac{19087}{60480} h^7 \sum_{j=1}^5 \frac{\partial f}{\partial y_j} \Big|_{y=y_p} y_j^{(7)} + \dots \quad (3.15a)$$

The error arising from the use of Eqs. (3.13) and (3.15a) is of order h^8 , but it is approximately 8.8 times larger than the last term in Eq. (3.13). For brevity we will refer to this method as PC76. To decrease the error because of the predicted value, y_p , one can use the AB7 method. Thus Eqs. (3.12) and (3.14) yield:

$$f(y_1) = f(y_p) + \frac{5257}{17280} h^8 \sum_{j=1}^5 \frac{\partial f}{\partial y_j} \Big|_{y=y_p} y_j^{(8)}(t) + \dots \quad (3.15b)$$

One sees that in this case because of the replacement of $f(y_1)$ with $f(y_p)$, the error in Eq. (3.13) is proportional to h^9 . Nevertheless, the ratio between the arising error and the last term in Eq. (3.13) is approximately equal to $8.5h$. Thus for $h < 0.1$, one can expect that the arising error will be of the order or smaller than the last term in Eq. (3.13). We will refer to this method as PC77.

4. Comparison of the numerical methods

4.1. Precision of the numerical schemes

To compare the precision of the numerical schemes, we used two sets of exact solutions of the problem: for each set, the dimensionless coordinates are denoted by $y_{1,th}(t), y_{2,th}(t)$, and $y_{3,th}(t)$. The error, $Err(t)$, is defined as follows:

$$Err(t) \equiv |y_1(t) - y_{1,th}(t)| + |y_2(t) - y_{2,th}(t)| + |y_3(t) - y_{3,th}(t)| \quad (4.1)$$

The simplest exact solution corresponds to a sphere of unit radius, $y_{1,th} = \sin t, y_{2,th} = 1 - \cos t, y_{3,th} = t$, which is obtained for $\epsilon_g = 0, \epsilon_\omega = 0$, and $b/d = 1$. Fig. 2a shows the calculated values of $Err(t)$ in the interval $t \in [0, 3.1]$ with a fixed step, $h = 0.1$. One sees that with the increase of the order of the Runge–Kutta method, the errors decrease for RK4 and RK5 and, as can be expected, for T6 the errors are considerably lower. In contrast, RK6 gives errors comparable to those for RK5 and the errors in the case of RK10 are much larger than those obtained with RK5. To clarify this result, we performed calculations with the RK6 and RK10 methods using the values of the functions at $t = 0.1$ predicted from the asymptotic expansions given in Appendix A as initial conditions and thus excluded the drop apex—the obtained results are denoted by RK6-1 and RK10-1 in Fig. 2a. Due to this modification, RK6-1 gives comparable errors with T6 and RK10-1 becomes the most precise method, except at the last point corresponding to $t = 3.1$. Therefore, the larger errors for RK6 and RK10 are observed because the Butcher tables of these methods use backward steps [29,30], which are not well-defined at the initial point, $t = 0$, see Eq. (3.4). The errors in the initial step of RK6 and RK10 affect the whole numerical solution and cause the considerable differences between RK6 vs. RK6-1 and RK10 vs. RK10-1, respectively. Even in the case of RK10-1, a sharp increase of the error is visible at the last point, $t = 3.1$, because of the small values of y_1 , see Eq. (3.4). The other methods considered here (RK4, RK5 [28], T6) use only forward steps and the obtained errors are predictable.

For this exact solution, the calculations using RK23 showed that the condition for the desired accuracy ϵ , Eq. (3.8), is more restrictive than the condition for stability, Eq. (3.9), for small ϵ . For example, if $\epsilon = 10^{-11}$ (see Fig. 2a) the real error is almost uniformly distributed across the whole interval, the largest one is $Err(3.1) \approx 10^{-10}$ and it is achieved for $h \approx 10^{-5}$. For this value of ϵ , the condition for stability is automatically fulfilled.

Fig. 2b shows the evolution of $Err(t)$ for the AB and PC methods. The initial steps needed to start the respective calculations are obtained using RK10-1. As can be expected, with the increase of the order of the methods, the errors decrease. The precision of AB6 and AB7 is lower than that of PC76 and PC77 becomes the most accurate

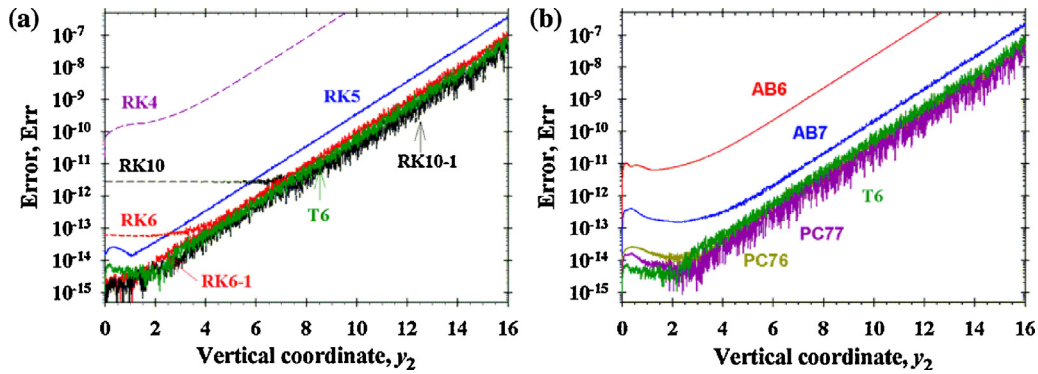


Fig. 3. Comparison of the precision of different numerical schemes for the limiting spinning drop profile calculated with $h=0.01$: (a) Taylor and Runge–Kutta methods; (b) Taylor, Adams–Bashforth and predictor-corrector methods.

method. It is evident from Fig. 2b that the seventh-order AB7, PC76, and PC77 methods have larger errors than the sixth-order methods T6 and RK6-1. It should be mentioned, however, that when the time step is smaller, $h=0.01$, the errors of PC76 and PC77 methods are comparable with those of T6 and RK6-1.

The second simple exact solution of the problem is obtained in Ref. [17] for a rotating drop ($\epsilon_\omega = 1$) in the absence of gravity ($\epsilon_g = 0$) and $b/d=1$. The corresponding expression for the limiting profile function reads [17]:

$$y_{2,\text{th}} = 3 - \sqrt{9 - y_{1,\text{th}}^2} + \frac{\sqrt{3}}{2} \left[\ln \left(\frac{2\sqrt{9 - y_{1,\text{th}}^2} + 3\sqrt{3}}{2\sqrt{9 - y_{1,\text{th}}^2} - 3\sqrt{3}} \right) - \ln \left(\frac{2 + \sqrt{3}}{2 - \sqrt{3}} \right) \right] \quad (3.17)$$

which is defined for $\Omega = 16/27$. We solved the initial value problem for $y_{1,\text{th}}$ and $y_{3,\text{th}}$ and obtained the following relationships:

$$y_{1,\text{th}} = \sqrt{\frac{9 \tanh^2(t/\sqrt{3})}{3 + \tanh^2(t/\sqrt{3})}} \quad \text{and} \quad y_{3,\text{th}} = \arcsin \left[y_{1,\text{th}} \left(1 - \frac{4y_{1,\text{th}}^2}{27} \right) \right] \quad (3.18)$$

Note that for $\Omega < 16/27$ the profiles have closed forms, which correspond to the typical spinning drop configurations (see Fig. 1c). In the opposite case, $\Omega > 16/27$, the capillary profiles are not closed.

Fig. 3 shows the calculated values of $\text{Err}(t)$ in the interval $y_2 \in [0, 16]$; the chosen step is $h=0.01$. The main difference between Figs. 2 and 3 is that the errors in Fig. 2 do not change considerably along the capillary profile, while those in Fig. 3 steadily increase. The behavior of the numerical algorithms RK4, RK5, and T6 (Fig. 3a) is analogous to that in Fig. 2a—the errors decrease with the increase of the order of the numerical scheme. The results for RK6 and RK10 illustrate the accumulation of the error in the initial step of calculations (Fig. 3a). Because of the increase of $\text{Err}(t)$ at larger values of y_2 , the differences between RK6 (RK10) and that started with the asymptotic solution at $t=0.01$ (Appendix A) RK6-1 (RK10-1) disappear.

The behavior of the AB and PC methods in the case of the limiting rotational profile solution (Fig. 3b) is different from that observed for a spherical profile (Fig. 2b). As can be expected, the errors for AB6 are the largest, followed by those for AB7. The methods PC76, PC77, and T6 give comparable results for $\text{Err}(t)$. Thus, from Fig. 3a and b, one can conclude that for the limiting spinning drop profile the precision of RK6-1, RK10-1, PC76, PC77, and T6 is comparable. For the calculations with RK23 and $\epsilon = 10^{-10}$, the step, h , which at the beginning of the interval is $h \approx 10^{-6}$, increases considerably at values of y_2 larger than 6 (in the almost horizontal profile of the solution) and the error grows to $\text{Err}(y_2=16) \approx 10^{-6}$. These special properties of the numerical schemes are due to the fact, that

$\Omega = 16/27$ is a critical parameter of the problem and determines a limiting solution.

4.2. Stability of the initial value problem

The precision and stability of the numerical schemes are of crucial importance for the data processing of experimental images in the case of rotating drops in gravitational field (see Fig. 1d and Section 5). If the experimental profile is significantly elongated, which is required to obtain better experimental precision, then small variations of the curvature at the apex lead to large deviations of the calculated profiles from the critical one.

One example is shown in Fig. 4a, where changes of b/d from unity with $\pm 10^{-4}$, $\pm 10^{-6}$, and $\pm 10^{-8}$ lead to the formation of closed profiles for $b/d < 1$ and open profiles for $b/d > 1$. These deviations are not because of numerical instability (RK6-1, RK10-1, PC76, PC77, and T6 give practically the same results with $h=0.01$)—they correspond to possible physical profiles. Therefore, if one knows the value of Ω and varies b/d in order to process well-elongated profiles, then one needs high precision numerical schemes because b/d is also a critical parameter for the problem and even values of $b/d = 1 \pm 10^{-8}$ cannot describe the limiting profile for $y_2 > 11$.

Small deviations from the limiting profile solution lead to jumps to other integral curves that deviate considerably from $y_{1,\text{th}}(y_{2,\text{th}})$. Fig. 4b shows the numerical results for $\Omega = 16/27$ and $b/d=1$. The following notation is used in Fig. 4b: A for RK23; B—RK5; C—AB7; D—RK6-1; E—PC76. For all methods with the exception of RK23 $h=0.01$. One sees that RK4 gives good results for $y_2 < 10$, while the other algorithms (except AB6 and RK23) are applicable up to $y_2 = 27$. The errors of the RK23 method are small up to $y_2 = 22$, but the step, h , is very small in the regions of large gradients, which increases the computational time. It is interesting to note that RK5 unexpectedly performs better than AB6, which does not work well for $y^2 > 21$.

5. Typical capillary profiles and data processing

5.1. Typical capillary profiles

Fig. 5a shows the obtained numerical results for a small rotating drop, for which the effect of gravity can be neglected. Curve 3 is a reference sphere of unit radius. Curves 1 and 2 correspond to $\epsilon_\omega = 1$ (spinning drop configurations) and curves 4 and 5 illustrate the opposite case $\epsilon_\omega = -1$ (“red blood cell” configurations). The volumes of all drops are equal to that of the reference sphere, $4/3$. In this case for a given value of Ω one varies b/d to obtain the drop with the defined volume. The respective parameters are: (1) $b/d=0.5192$, $\Omega=4.214$; (2) $b/d=0.6647$, $\Omega=1.873$; (4) $d/b=0$, $\Omega=2.004$; (5) $b/d=-1.333$, $\Omega=2.112$. For $\epsilon_\omega = 1$, the drop becomes more elongated with the increase of angular velocity ω , which

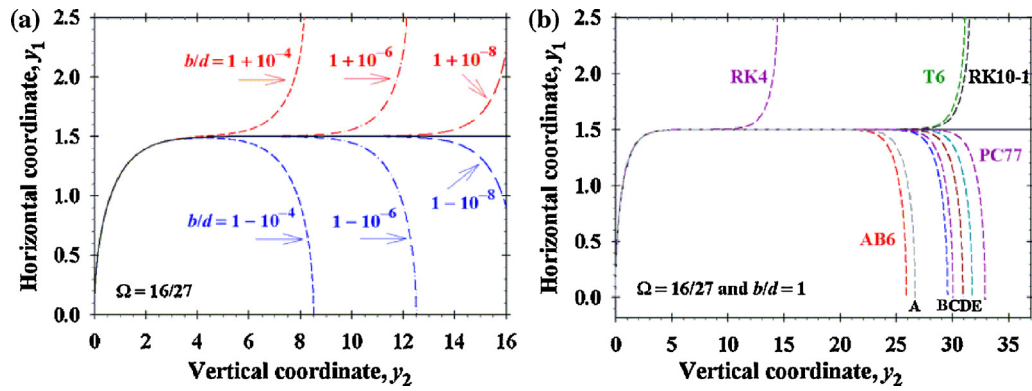


Fig. 4. Deviations of the numerical solutions from the limiting profile function given by Eqs. (3.17) and (3.18) (solid line): (a) because of small variations of the curvature at the apex, b/d , at fixed $\Omega = 16/27$; (b) because of the errors in the numerical schemes. A small changes of b/d or the errors in the numerical schemes can cause a jump to another integral curve.

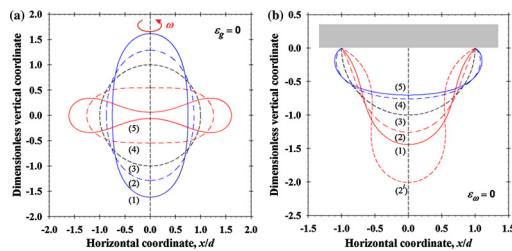


Fig. 5. Typical capillary profiles. (a) Rotating drops without gravity ($\epsilon_g = 0$): (1) and (2)—spinning drop configurations; (4) and (5)—“red blood cell” configurations. (b) Without centrifugal field ($\epsilon_\omega = 0$): (1), (2), and (2')—pendant drop configurations; (4) and (5)—sessile bubble configurations. The dimensionless vertical coordinate for each curve is shifted for better visibility.

corresponds to the main idea of spinning drop tensiometry. For $\epsilon_\omega = -1$, the shape with zero curvature at the drop apex is observed for $\epsilon_\omega = -1$ and $\Omega = 2.004$. Further increase of the angular velocity, ω , leads to the formation of toroidal shapes with dimples.

Fig. 5b illustrates the typical capillary profiles for pendant drops ($\epsilon_g = -1$, curves 1, 2 and 2') and sessile bubbles ($\epsilon_g = 1$, curves 4 and 5) without applied centrifugal field ($\epsilon_\omega = 0$). Curve 3 is a reference hemisphere of unit radius. The volumes of all drops/bubbles are equal to that of the reference hemisphere, $2/3$. In this case one defines B and varies b/d to obtain the configuration with volume $2/3$. The dimensionless parameters of the profiles are: (1) $b/d = 0.5424$, $B = 2.9$; (2) $b/d = 0.6350$, $B = 2.4$; (2') $b/d = 0.4844$, $B = 2.4$; (4) $b/d = 2.554$, $B = 6.0$; (5) $b/d = 3.397$, $B = 8.0$. As can be expected, to obtain pendant drops with the same volume, the necessary increase of the Bond number is much smaller than that needed to deform sessile bubbles because of the different vertical distances, see Eq. (3.2) where the right-hand side includes the term By^2 . It is interesting to note that two or more pendant drop configurations with a fixed volume and Bond number can be realized numerically (see curves 2 and 2'). For practical applications, the solutions with a neck (curve 2') are not interesting because of the instability of such capillary profiles [36,40,41]. More precisely, the capillary profiles, which contain an inflection point, are physically unstable.

Fig. 6a illustrates the effect of the centrifugal field on the profiles of pendant drops (curves 1–3, $\epsilon_g = -1$, $\epsilon_\omega = -1$) and on sessile bubbles (curves 4–6, $\epsilon_g = 1$, $\epsilon_\omega = 1$). In both of these cases, the gravitational and centrifugal fields act in opposite directions, which stabilizes the capillary shapes. All bubbles and drops are of dimensionless volume $2/3$. Curve 1 in Fig. 6a is the same as curve 1 in Fig. 5b and is calculated with $b/d = 0.5424$ and $B = 2.9$. Applying a centrifugal field with a higher value of Ω stabilizes the drop pro-

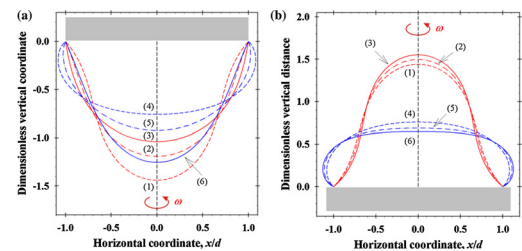


Fig. 6. Typical capillary profiles. (a) Rotating pendant drops and sessile bubbles—the dimensionless vertical coordinate for each curve is shifted for better visibility. (b) Rotating buoyant bubbles and sessile drops—the dimensionless vertical distance is measured from the solid substrate. For more details see the text.

files (see curves 2 and 3 in Fig. 6a). The respective parameters are: (2) $b/d = 0.7050$, $\Omega = 1.0$; (3) $b/d = 0.9782$, $\Omega = 2.0$. Curves 4 in Figs. 6a and 5b are identical and correspond to $b/d = 2.554$ and $B = 6.0$. With the increase of the angular velocity, ω , the bubble profiles become elongated and smooth (curves 5 and 6 are calculated with $b/d = 1.114$, $\Omega = 3.0$, and $b/d = 0.5461$, $\Omega = 11.0$, respectively).

Fig. 6b demonstrates the destabilizing effect the applied centrifugal field has when it acts in the same direction as gravity. Curves 1–3 correspond to the calculated results for buoyant bubbles ($\epsilon_g = -1$, $\epsilon_\omega = 1$) and curves 4–6—to sessile drops ($\epsilon_g = 1$, $\epsilon_\omega = -1$). The buoyant bubbles have the same configuration as the pendant drops and curves 1 and 4 correspond to those in Fig. 5b. A small increase of the angular velocity, ω , leads to destabilization of the profiles and these configurations are not convenient for experimental equipment. The parameters of the curves are: (2) $b/d = 0.5246$, $\Omega = 0.1$; (3) $b/d = 0.5098$, $\Omega = 0.15$; (5) $b/d = 5.219$, $\Omega = 1.0$; (6) $b/d = 11.92$, $\Omega = 1.5$.

5.2. Processing of experimental data

In the conventional case of ADSA (Fig. 1a and b), the computer image of the drop is processed to obtain the experimental drop profile coordinates.

For example, Fig. 7a shows the digitalized experimental profile of a pendant drop. The coordinates are scaled with the capillary tip radius, $d = r_c$. The density difference and the gravitational acceleration are known, so that the adjustable parameters are the surface tension expressed in terms of the Bond number, B , and the dimensionless radius of curvature, b/d . Moreover, a relatively precise initial value of b/d can be obtained from geometrical considerations because the capillary profile around the drop apex is approximated relatively well with a sphere. The order of magnitude of the initial value of B is also known because the order of the magnitude

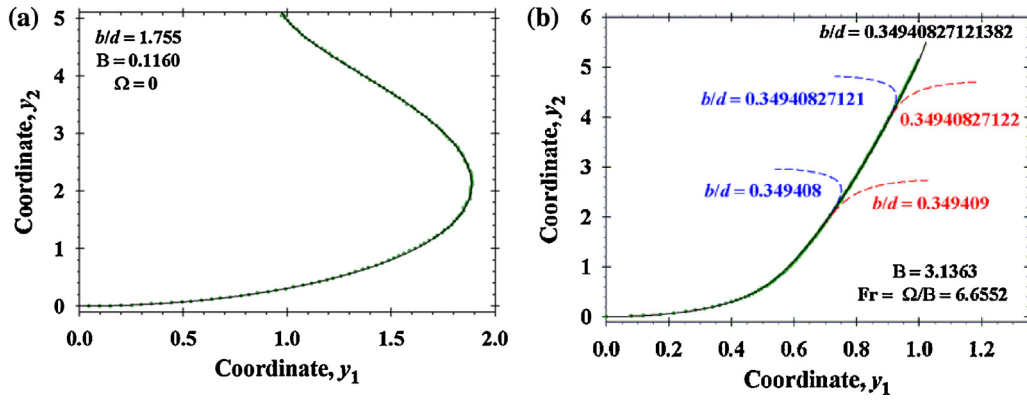


Fig. 7. Results from the data processing of experimental images. (a) Pendant drop – the best fit is obtained with $B=0.1160$ and $b/d=1.755$ (solid line); the points correspond to experimental data. (b) Rotating drop in gravitational field ($\epsilon_\omega = 1$ and $\epsilon_g = 1$)—the best fit is obtained with $B=3.1363$ and $b/d=0.34940827121382$ (solid line); the points correspond to experimental data; the short-dash lines are calculated with $Fr=6.6552$ and different values of b/d .

of the interfacial tension, σ , is known. In this case, the initial value problem is stable, all considered numerical schemes are applicable, and the processing of the drop profile is fast enough. The obtained results are $B=0.1160$ and $b/d=1.755$ (see Fig. 7a)—more accurate values of B and b/d cannot be calculated because of the experimental errors. More details about the precision and accuracy of the method are discussed in Refs. [7,15].

For rotating drops in a gravitational field, the data processing is more complicated. In this case, the density difference ($\Delta\rho$), the gravitational acceleration (g), and the rotational velocity (ω) are known. Note that to process data for a digitalized drop profile (Fig. 7b), one again needs only two parameters—those are b/d ($d=r_c$) and B . The value of Ω is not known, but it can be expressed via the rotational Froude number, $Fr = \Omega/B = \omega^2 d/(2g)$, which is known. For a given value of B , to obtain the elongated profiles one needs to adjust b/d with a very high accuracy. Fig. 7b shows the obtained best fit (solid line) of the experimental profile (dots) with $\epsilon_\omega = 1$, $B=3.1363$ and $b/d=0.34940827121382$ using the T6 method with $h=0.01$. Note that for a fixed value of $B=3.1363$ changes in the sixth digit of b/d lead to considerable deviations of the calculated profiles from the experimental one. Even changes in the eleventh digit of b/d have an effect on the differences between the calculated and experimental profiles close to the capillary tip. For that reason, to obtain the best-fit profile, one needs numerical schemes of very high precision and good stability. We checked whether the decrease of the values of h changes the obtained numerical results and found no effect for the methods used here (except RK23, AB6, and AB7). It is important to note, that the calculated capillary profiles are extremely sensitive to the values of b/d because of the numerical schemes. From physical viewpoint the important parameter is the Bond number, B , needed to measure the interfacial tension. The precision of B depends on the resolution of images and the deformation of the drop/bubble. In our case the relative error of B obtained from the minimization procedure is about 0.1%.

To accelerate the minimizing procedure, one needs a good initial guess. For that reason, dealing with the case $\epsilon_\omega = 1$, we represent Eq. (2.6) in the following form:

$$\sin\theta = \frac{r}{b} - \frac{\Delta\rho}{8\sigma}\omega^2 r^3 + \epsilon_g \frac{g\Delta\rho}{r\sigma} \int_0^r z(\tilde{r})\tilde{r}d\tilde{r} \quad (5.1)$$

which corresponds to elongated drop profiles. Note that the integral in the right-hand side of Eq. (5.1) is evaluated for a single-valued function, $z(\tilde{r})$, which is the typical experimental case. In the inflec-

tion point, the derivative of $\sin\theta$ with respect to r is equal to zero, so that from Eq. (5.1) one obtains:

$$\frac{1}{b} = \frac{3\Delta\rho}{8\sigma}\omega^2 r_{\text{inf}}^2 - \epsilon_g \frac{g\Delta\rho}{\sigma} z_{\text{inf}} + \epsilon_g \frac{g\Delta\rho}{r_{\text{inf}}^2 \sigma} \int_0^{r_{\text{inf}}} z(\tilde{r})\tilde{r}d\tilde{r} \quad (5.2)$$

where the subscript “inf” refers to the respective coordinates calculated at the inflection point. The substitution of Eq. (5.2) into (5.1) leads to the following result:

$$\sin\theta_{\text{inf}} = \frac{\Delta\rho}{4\sigma}\omega^2 r_{\text{inf}}^3 - \epsilon_g \frac{g\Delta\rho}{r_{\text{inf}}\sigma} \int_0^{z_{\text{inf}}} r^2(\tilde{z})d\tilde{z} \quad (5.3)$$

If the drop is elongated enough, then at the inflection point $\theta_{\text{inf}} \approx \pi/2$, and one obtains the approximate expression:

$$\sigma \approx \frac{\Delta\rho}{4}\omega^2 r_{\text{inf}}^3 - \epsilon_g \frac{g\Delta\rho}{r_{\text{inf}}} \int_0^{z_{\text{inf}}} r^2(\tilde{z})d\tilde{z} \quad (5.4)$$

Eq. (5.4) in the case of $g=0$ reduces to the Vonnegut formula [16] for calculation of the interfacial tension via the spinning drop method. To estimate the initial values of b/d and B , needed for the data processing of the image shown in Fig. 7b, we represent Eq. (5.4) in its dimensionless form using $\epsilon_g = 1$ and the definitions of the dimensionless parameters (see Section 3):

$$\frac{1}{B} \approx \frac{Fr}{2} - V_c \quad \text{and} \quad V_c \equiv \int_0^{y_{2,c}} y_1^2(y_2)dy_2 \quad (5.5)$$

Note that because the radial and vertical coordinates of the capillary tip are r_c and z_c , respectively, and $d=r_c$, at this point we have $y_{1,c} = 1$ and $y_{2,c} = z_c/r_c$. The integral in the right-hand side of Eq. (5.5), V_c , is calculated directly from the experimental data. In our case (Fig. 7b), we have $Fr = 6.6552$ and $V_c = 2.9959$, so that Eq. (5.5) gives the initial value of $B=3.0148$, which is very close to the best-fit result of $B=3.1363$.

The second step is to rewrite Eq. (5.2) in its equivalent form:

$$\frac{1}{b} = \frac{3\Delta\rho}{8\sigma}\omega^2 r_{\text{inf}}^2 - \epsilon_g \frac{g\Delta\rho}{2\sigma} z_{\text{inf}} - \epsilon_g \frac{g\Delta\rho}{2r_{\text{inf}}^2 \sigma} \int_0^{z_{\text{inf}}} \tilde{r}^2(\tilde{z})d\tilde{z} \quad (5.6)$$

Table 1
Computational time of different numerical methods and the best values of b/d .

Method	Time (ms)	b/d
AB6	8	0.34940827149531
AB7	8	0.34940827121620
PC76	17	0.34940827121496
PC77	17	0.34940827121331
T6	17	0.34940827121382
RK4	21	0.34940827224377
RK5	30	0.34940827121356
RK6-1	40	0.34940827121364
RK10-1	160	0.34940827121364

It is more convenient to express Eq. (5.6) in dimensionless form, which in terms of our approximations is equivalent to:

$$\frac{d}{b} \approx \frac{B}{2} \left(\frac{3}{2} \text{Fr} - y_{2,c} - V_c \right) \quad (5.7)$$

Using the experimental value of $y_{2,c} = 5.16$ and the initial quest of $B = 3.0148$, we calculate the initial value of b/d to be 0.36312, which is close to the best-fit result. Therefore, Eqs. (5.5) and (5.7) can be used as an excellent initial guess for the minimization procedure.

5.3. Computational time

To compare the computational time of the considered methods, we repeated the calculations of the best-fit profile in Fig. 7b 100 times. In all numerical schemes (except for RK23) we used a fixed step, h , equal to 0.01 and the number of steps for one profile was approximately equal to 544. In the case of RK23, the computational time was much longer than those for the other algorithms, because of the considerable decrease of the step, h , required in order to achieve the needed accuracy. All programs were written on PC using Fortran and double precision. The Butcher parameters and all coefficients in T6, AB6, AB7, PC76, and PC77 were used as double precision constants.

Table 1 summarizes the values of the computational times and the best-fit parameters, b/d . First, the values of b/d are the same for all methods except for AB6 and RK4, most probably because of the different accuracy of these methods (see Fig. 4b). Nevertheless, all calculated profiles are identical up to relative deviations of less than 10^{-4} , which are considerably lower than the experimental error of the digitalization procedure. Second, the Runge–Kutta methods are slower than the other methods because of the large number of stages—for example, RK10 has 17 stages. As can be expected the computational times of AB6 and AB7 are equal and the shortest—about 2 times shorter than those of T6, PC76, and PC77. From the viewpoint of real-time data processing it seems that T6, PC76, and PC77 are the most appropriate methods because of their sufficiently short computational times, good accuracy and stability.

6. Conclusions

This paper investigates the applicability of different numerical methods (Runge–Kutta, Taylor, Adams–Bashforth, and predictor–corrector) for the data processing of images of drops/bubbles in gravitational and centrifugal fields. Because of the action of the centrifugal field, the drops become well-elongated and to reproduce their experimental profiles, the curvature at the drop apex, b , should be calculated with very high precision (with relative error of less than 10^{-12}). The additional requirements imposed upon numerical methods for real-time data processing are to have good stability with respect to variation of the parameters controlling the capillary profiles and a short and fixed computational time.

The numerical experiments show that for the problems, considered here, the more restrictive condition for the second-order

3-stage explicit Runge–Kutta method with step control (RK23) is that for the accuracy, Eq. (3.8). This particularly concerns the instances when some parameters are critical for the problems and for the behavior of their solutions. In our case, these are the problems for a rotating drop in the absence of gravity and in a gravitational field (the critical parameter for both cases is b/d). For conventional ADSA (without rotation), the RK23 method is applicable and gives excellent results. This conclusion is valid not only for RK23, but also for the classes of Runge–Kutta methods with step size control, for example RK45.

The sixth- and seventh- order Adams–Bashforth explicit methods (AB6 and AB7) have the shortest computational time but lower precision compared to the other studied methods. The best results for the specific problem we achieved with the sixth-order Taylor method (T6) and the predictor–corrector numerical methods (PC76 and PC77) based on the seventh-order implicit Adams–Moulton expansion using as a predictor the results from AB6 or AB7. We recommend one of these 3 numerical methods (T6, PC76, and PC77) to be implemented in equipment for the measurement of the interfacial tension, via shape analysis of capillary profiles subjected to both gravitational and centrifugal fields because of their stability and sufficiency short computational times.

The Runge–Kutta methods (Cash and Karp fifth-order [28], Verner sixth-order [29], and Feagin tenth-order [30]) combined with the initial step calculated from the series expansion of the solution up to the tenth-order (see Appendix A) are stable and applicable for data processing. However, these methods are much more time-consuming than T6, PC76, and PC77.

Acknowledgements

The work of SD is partially supported under Grant I02/9, 12.12.2014, by NSF of the Bulgarian Ministry of Education and Science. KD gratefully acknowledges the support from the ESF COST Action CM1101. The work of TI is partially supported by Sofia University Science Found under Grand 75/2015.

Appendix A.

Formulas for the derivatives used in the explicit Taylor method

As usual, the values of the first derivatives are calculated directly from the right-hand side of Eq. (3.2). From Eq. (3.3) one sees that $y_4^{(j)}$ is simply related to $y_1^{(j)}$: $y_4^{(j)} = y_1^{(j-1)}$ ($j = 1, 2, \dots$). In order to avoid possible confusion between derivatives and powers in the formula below, we use the following notation:

$$y_{k,0} \equiv y_k, y_{k,j} \equiv y_k^{(j)} \quad (k = 1, \dots, 5 \text{ and } j = 1, 2, \dots) \quad (A.1)$$

Second-order precision

Differentiating Eqs. (3.2)–(3.4) with respect to t , we obtain:

$$y_{1,2} = -y_{2,1}y_{3,1}, y_{2,2} = y_{1,1}y_{3,1} \quad (A.2)$$

$$y_{3,2} = \frac{y_{1,1}y_{2,1}}{y_{1,0}^2} - \frac{y_{2,2}}{y_{1,0}} - 2\epsilon_\omega \Omega y_{1,0}y_{1,1} + \epsilon_g B y_{2,1} \quad (A.3)$$

$$y_{5,2} = 2y_{1,0}y_{1,1}y_{2,1} + y_{1,0}^2 y_{2,2} \quad (A.4)$$

For $\Omega = 0$ Eqs. (A.2) and (A.3) are reported in Refs. [5,40,41].

Third-order precision

Taking the second derivative of Eqs. (3.2)–(3.4) with respect to t , we calculate:

$$y_{1,3} = -y_{2,2}y_{3,1} - y_{2,1}y_{3,2}, y_{2,3} = y_{1,2}y_{3,1} + y_{1,1}y_{3,2} \quad (A.5)$$

$$y_{3,3} = -2 \frac{y_{1,1}^2 y_{2,1}}{y_{1,0}^3} + \frac{y_{1,2} y_{2,1} + 2y_{1,1} y_{2,2}}{y_{1,0}^2} - \frac{y_{2,3}}{y_{1,0}} - 2\epsilon_\omega \Omega (y_{1,1}^2 + y_{1,0} y_{1,2}) + \epsilon_g B y_{2,2} \quad (\text{A.6})$$

$$y_{5,3} = 2y_{1,1}^2 y_{2,1} + 2y_{1,0} y_{1,2} y_{2,1} + 4y_{1,0} y_{1,1} y_{2,2} + y_{1,0}^2 y_{2,3} \quad (\text{A.7})$$

Fourth-order precision

Taking the third derivative of Eqs. (3.2)–(3.4) with respect to t leads to the expressions:

$$y_{1,4} = -y_{2,3} y_{3,1} - 2y_{2,2} y_{3,2} - y_{2,1} y_{3,3}, y_{2,4} = y_{1,3} y_{3,1} + 2y_{1,2} y_{3,2} + y_{1,1} y_{3,3} \quad (\text{A.8})$$

$$y_{3,4} = 6 \frac{y_{1,1}^3 y_{2,1}}{y_{1,0}^4} - 6 \frac{y_{1,1} y_{1,2} y_{2,1} + y_{1,1}^2 y_{2,2}}{y_{1,0}^3} + \frac{y_{1,3} y_{2,1} + 3y_{1,2} y_{2,2} + 3y_{1,1} y_{2,3}}{y_{1,0}^2} - \frac{y_{2,4}}{y_{1,0}} - 2\epsilon_\omega \Omega (3y_{1,1} y_{1,2} + y_{1,0} y_{1,3}) + \epsilon_g B y_{2,3} \quad (\text{A.9})$$

$$y_{5,4} = 6y_{1,1} y_{1,2} y_{2,1} + 2y_{1,0} y_{1,3} y_{2,1} + 6y_{1,1}^2 y_{2,2} + 6y_{1,0} y_{1,2} y_{2,2} + 6y_{1,0} y_{1,1} y_{2,3} + y_{1,0}^2 y_{2,4} \quad (\text{A.10})$$

Fifth-order precision

The fourth derivative of Eqs. (3.2)–(3.4) with respect to t gives the formulas:

$$y_{1,5} = -y_{2,4} y_{3,1} - 3y_{2,3} y_{3,2} - 3y_{2,2} y_{3,3} - y_{2,1} y_{3,4} \quad (\text{A.11})$$

$$y_{2,5} = y_{1,4} y_{3,1} + 3y_{1,3} y_{3,2} + 3y_{1,2} y_{3,3} + y_{1,1} y_{3,4} \quad (\text{A.12})$$

$$y_{3,5} = -24 \frac{y_{1,1}^4 y_{2,1}}{y_{1,0}^5} + 12 \frac{3y_{1,1}^2 y_{1,2} y_{2,1} + 2y_{1,1}^3 y_{2,2}}{y_{1,0}^4} - 2 \frac{3y_{1,2}^2 y_{2,1} + 4y_{1,1} y_{1,3} y_{2,1} + 12y_{1,1} y_{1,2} y_{2,2} + 6y_{1,1}^2 y_{2,3}}{y_{1,0}^3} + \frac{y_{1,4} y_{2,1} + 4y_{1,3} y_{2,2} + 6y_{1,2} y_{2,3} + 4y_{1,1} y_{2,4}}{y_{1,0}^2} - \frac{y_{2,5}}{y_{1,0}} - 2\epsilon_\omega \Omega (3y_{1,2}^2 + 4y_{1,1} y_{1,3} + y_{1,0} y_{1,4}) + \epsilon_g B y_{2,4} \quad (\text{A.13})$$

$$y_{5,5} = 6y_{1,2}^2 y_{2,1} + 8y_{1,1} y_{1,3} y_{2,1} + 2y_{1,0} y_{1,4} y_{2,1} + 24y_{1,1} y_{1,2} y_{2,2} + 8y_{1,0} y_{1,3} y_{2,2} + 12y_{1,0} y_{1,2} y_{2,3} + 12y_{1,1}^2 y_{2,3} + 8y_{1,0} y_{1,1} y_{2,4} + y_{1,0}^2 y_{2,5} \quad (\text{A.14})$$

Sixth-order precision

Finally, from the fifth derivative with respect to t of Eqs. (3.2)–(3.4), we derive:

$$y_{1,6} = -y_{2,5} y_{3,1} - 4y_{2,4} y_{3,2} - 6y_{2,3} y_{3,3} - 4y_{2,2} y_{3,4} - y_{2,1} y_{3,5} \quad (\text{A.15})$$

$$y_{2,6} = y_{1,5} y_{3,1} + 4y_{1,4} y_{3,2} + 6y_{1,3} y_{3,3} + 4y_{1,2} y_{3,4} + y_{1,1} y_{3,5} \quad (\text{A.16})$$

$$y_{3,6} = 120 \frac{y_{1,1}^5 y_{2,1}}{y_{1,0}^6} - 120 \frac{2y_{1,1}^3 y_{1,2} y_{2,1} + y_{1,1}^4 y_{2,2}}{y_{1,0}^5} + 6 \frac{15y_{1,1} y_{1,2}^2 y_{2,1} + 10y_{1,1}^2 y_{1,3} y_{2,1} + 30y_{1,1}^2 y_{1,2} y_{2,2} + 10y_{1,1}^3 y_{2,3}}{y_{1,0}^4} - 2 \frac{10y_{1,2} y_{1,3} y_{2,1} + 5y_{1,1} y_{1,4} y_{2,1} + 15y_{1,2}^2 y_{2,2} + 20y_{1,1} y_{1,3} y_{2,2} + 30y_{1,1} y_{1,2} y_{2,3} + 10y_{1,1}^2 y_{2,4}}{y_{1,0}^3} + \frac{y_{1,5} y_{2,1} + 5y_{1,4} y_{2,2} + 10y_{1,3} y_{2,3} + 10y_{1,2} y_{2,4} + 5y_{1,1} y_{2,5}}{y_{1,0}^2} - \frac{y_{2,6}}{y_{1,0}} - 2\epsilon_\omega \Omega (10y_{1,2} y_{1,3} + 5y_{1,1} y_{1,4} + y_{1,0} y_{1,5}) + \epsilon_g B y_{2,5} \quad (\text{A.17})$$

$$y_{5,6} = 20y_{1,2} y_{1,3} y_{2,1} + 10y_{1,1} y_{1,4} y_{2,1} + 2y_{1,0} y_{1,5} y_{2,1} + 30y_{1,2}^2 y_{2,2} + 40y_{1,1} y_{1,3} y_{2,2} + 10y_{1,0} y_{1,4} y_{2,2} + 60y_{1,1} y_{1,2} y_{2,3} + 20y_{1,0} y_{1,3} y_{2,3} + 20y_{1,0} y_{1,2} y_{2,4} + 20y_{1,1}^2 y_{2,4} + 10y_{1,0} y_{1,1} y_{2,5} + y_{1,0}^2 y_{2,6} \quad (\text{A.18})$$

First step of the algorithm

The right-hand side of Eq. (3.2) is not defined at $r=0$. For this reason, we expand the solution in a series around the drop apex to calculate the values of the functions needed to start the first step of the algorithm. We define the rescaled parameters \tilde{B} and $\tilde{\Omega}$ as follows:

$$\tilde{B} \equiv \epsilon_g B \frac{b^2}{d^2} \quad \text{and} \quad \tilde{\Omega} \equiv \epsilon_\omega \Omega \frac{b^3}{d^3} \quad (\text{A.19})$$

The obtained results for the respective series read:

$$y_1(h) = h - \frac{d^2 h^3}{6b^2} + \frac{d^4 h^5}{120b^4} (1 - 3\tilde{B} + 6\tilde{\Omega}) + \frac{d^6 h^7}{40320b^6} (-8 + 144\tilde{B} - 75\tilde{B}^2 - 528\tilde{\Omega} + 240\tilde{B}\tilde{\Omega} - 180\tilde{\Omega}^2) + \frac{d^8 h^9}{2903040b^8} (8 - 648\tilde{B} + 1972\tilde{B}^2 - 245\tilde{B}^3 + 4896\tilde{\Omega} - 10488\tilde{B}\tilde{\Omega} + 910\tilde{B}^2\tilde{\Omega} + 12528\tilde{\Omega}^2 - 840\tilde{B}\tilde{\Omega}^2) + o(h^{10}) \quad (\text{A.20})$$

$$y_2(h) = \frac{dh^2}{2b} - \frac{d^3 h^4}{24b^3} (1 - \frac{3}{4}\tilde{B} + \frac{3}{2}\tilde{\Omega}) + \frac{d^5 h^6}{720b^5} (1 - 8\tilde{B} + \frac{5}{8}\tilde{B}^2 + 21\tilde{\Omega} - \frac{5}{4}\tilde{B}\tilde{\Omega}) - \frac{d^7 h^8}{2580480b^7} (64 - 2440\tilde{B} + 3624\tilde{B}^2 - 35\tilde{B}^3 + 12960\tilde{\Omega} - 14296\tilde{B}\tilde{\Omega} + 70\tilde{B}^2\tilde{\Omega} + 13536\tilde{\Omega}^2) - \frac{d^9 h^{10}}{464486400b^9} (-128 + 21888\tilde{B} - 118792\tilde{B}^2 + 51776\tilde{B}^3 - 63\tilde{B}^4 - 235776\tilde{\Omega} + 862368\tilde{B}\tilde{\Omega} - 247720\tilde{B}^2\tilde{\Omega} + 126\tilde{B}^3\tilde{\Omega} - 1237248\tilde{\Omega}^2 + 365088\tilde{B}\tilde{\Omega}^2 - 155520\tilde{\Omega}^3) + o(h^{10}) \quad (\text{A.21})$$

$$\begin{aligned}
y_3(h) = & \frac{dh}{b} + \frac{d^3h^3}{8b^3}(\tilde{B} - 2\tilde{\Omega}) - \frac{d^5h^5}{240b^5}(\tilde{B} - \frac{5}{4}\tilde{B}^2 - 12\tilde{\Omega} + \frac{5}{2}\tilde{B}\tilde{\Omega}) \\
& + \frac{d^7h^7}{322560b^7}(88\tilde{B} - 264\tilde{B}^2 + 35\tilde{B}^3 - 1536\tilde{\Omega} + 2536\tilde{B}\tilde{\Omega} \\
& - 70\tilde{B}^2\tilde{\Omega} - 3456\tilde{\Omega}^2) + \frac{d^9h^9}{46448640b^9}(576\tilde{B} + 5032\tilde{B}^2 \\
& - 3896\tilde{B}^3 + 63\tilde{B}^4 + 12288\tilde{\Omega} - 79008\tilde{B}\tilde{\Omega} + 31000\tilde{B}^2\tilde{\Omega} \\
& - 126\tilde{B}^3\tilde{\Omega} + 165888\tilde{\Omega}^2 - 62688\tilde{B}\tilde{\Omega}^2 + 34560\tilde{\Omega}^3) + o(h^{10})
\end{aligned} \tag{A.22}$$

$$\begin{aligned}
y_4(h) = & \frac{h^2}{2} - \frac{d^2h^4}{24b^2} + \frac{d^4h^6}{720b^4}(1 - 3\tilde{B} + 6\tilde{\Omega}) \\
& + \frac{d^6h^8}{322560b^6}(-8 + 144\tilde{B} - 75\tilde{B}^2 - 528\tilde{\Omega} \\
& + 240\tilde{B}\tilde{\Omega} - 180\tilde{\Omega}^2) + \frac{d^8h^{10}}{29030400b^8}(8 - 648\tilde{B} + 1972\tilde{B}^2 \\
& - 245\tilde{B}^3 + 4896\tilde{\Omega} - 10488\tilde{B}\tilde{\Omega} + 910\tilde{B}^2\tilde{\Omega} + 12528\tilde{\Omega}^2 \\
& - 840\tilde{B}\tilde{\Omega}^2) + o(h^{10})
\end{aligned} \tag{A.23}$$

$$\begin{aligned}
y_5(h) = & \frac{dh^4}{4b} - \frac{d^3h^6}{48b^3}(4 - \tilde{B} + 2\tilde{\Omega}) + \frac{d^5h^8}{7680b^5}(104 - 152\tilde{B} + 5\tilde{B}^2 \\
& + 344\tilde{\Omega} - 10\tilde{B}\tilde{\Omega}) + \frac{d^7h^{10}}{1935360b^7}(-2624 + 11448\tilde{B} \\
& - 4440\tilde{B}^2 + 21\tilde{B}^3 - 32736\tilde{\Omega} + 16392\tilde{B}\tilde{\Omega} - 42\tilde{B}^2\tilde{\Omega} \\
& - 14688\tilde{\Omega}^2) + o(h^{10})
\end{aligned} \tag{A.24}$$

Eqs. (A.20)–(A.24) are used to calculate the values of the approximate solution at the initial step with the appropriate precision corresponding to the applied numerical scheme.

References

- [1] F. Bashforth, C. Adams, *An Attempt to Test the Theories of Capillary Action*, Cambridge Univ. Press, Cambridge, 1892.
- [2] J.M. Andreas, E.A. Hauser, W.B. Tucker, Boundary tension by pendant drops, *J. Phys. Chem.* 42 (1938) 1001–1019.
- [3] S. Fordham, On the calculation of surface tension from measurements of pendant drops, *Proc. R. Soc. Lond. A* 194 (1948) 1–16.
- [4] A.I. Rusanov, V.A. Prokhorov, *Interfacial Tensiometry*, Elsevier, Amsterdam, 1996.
- [5] Y. Rotenberg, I. Boruvka, A.W. Neumann, Determination of surface tension and contact angle from the shapes of axisymmetric fluid interfaces, *J. Colloid Interface Sci.* 93 (1983) 169–183.
- [6] J.K. Ferri, S.Y. Lin, K.J. Stebe, Curvature effects in the analysis of pendant bubble data: comparison of numerical solutions, asymptotic arguments, and data, *J. Colloid Interface Sci.* 241 (2001) 154–168.
- [7] M. Hoorfar, A.W. Neumann, Recent progress in axisymmetric drop shape analysis (ADSA), *Adv. Colloid Interface Sci.* 121 (2006) 25–49.
- [8] S.A. Zholob, A.V. Makievski, R. Miller, V.B. Fainerman, Optimisation of calculation methods of surface tension by drop profile analysis tensiometry, *Adv. Colloid Interface Sci.* 134 (2007) 322–329.
- [9] F. Ravera, G. Loglio, V.I. Kovalchuk, Interfacial dilatational rheology by oscillating bubble/drop methods, *Curr. Opin. Colloid Interface Sci.* 15 (2010) 217–228.
- [10] O.I. del Río, A.W. Neumann, Axisymmetric drop shape analysis: computational methods for the measurements of interfacial properties from the shape and dimensions of pendant and sessile drops, *J. Colloid Interface Sci.* 196 (1997) 136–147.
- [11] H. Tavana, A.W. Neumann, Recent progress in the determination of solid surface tensions from contact angles, *Adv. Colloid Interface Sci.* 132 (2007) 1–32.
- [12] A.F. Stalder, T. Melchior, M. Müller, D. Sage, T. Blu, M. Unser, Low-bond axisymmetric drop shape analysis for surface tension and contact angle measurements of sessile drops, *Colloids Surf. A* 364 (2010) 72–81.
- [13] P.A. Kralchevsky, K.D. Danov, V.L. Kolev, T.D. Gurkov, M.L. Temelska, G. Brenn, Detachment of oil drops from solid surfaces in surfactant solutions: molecular mechanism at a moving contact line, *Ind. Eng. Chem. Res.* 44 (2005) 1309–1321.
- [14] V.L. Kolev, I.I. Kochijashky, K.D. Danov, P.A. Kralchevsky, G. Broze, A. Mehreteab, Spontaneous detachment of oil drops from solid substrates: governing factors, *J. Colloid Interface Sci.* 257 (2003) 357–363.
- [15] A. Kalantarian, S.M.I. Saad, A.W. Neumann, Accuracy of surface tension measurement from drop shapes: the role of image analysis, *Adv. Colloid Interface Sci.* 199–200 (2013) 15–22.
- [16] B. Vonnegut, Rotating bubble method for the determination of surface and interfacial tensions, *Rev. Sci. Instrum.* 13 (1942) 6–9.
- [17] H.M. Princen, I.Y.Z. Zia, S.G. Mason, Measurement of interfacial tension from the shape of a rotating drop, *J. Colloid Interface Sci.* 23 (1967) 99–107.
- [18] C.D. Manning, L.E. Scriven, On interfacial tension measurements with a spinning drop in gyrostatic equilibrium, *Rev. Sci. Instrum.* 48 (1977) 1699–1705.
- [19] H.H. Hu, D.D. Joseph, Evolution of a liquid drop in a spinning drop tensiometer, *J. Colloid Interface Sci.* 162 (1994) 331–339.
- [20] F.D. Rumscheidt, S.G. Mason, Break-up of stationary liquid threads, *J. Colloid Interface Sci.* 17 (1962) 260–269.
- [21] M.P. Aronson, H.M. Princen, Shape of a meniscus in a rotating vertical tube, *J. Chem. Soc. Faraday Trans. 1* 74 (1978) 555–574.
- [22] V.A. Lubarda, K.A. Talke, Configurational forces and shape of a sessile droplet on a rotating solid substrate, *Theor. Appl. Mech.* 39 (2012) 27–54.
- [23] J.C. Butcher, A history of Runge–Kutta methods, *Appl. Num. Math.* 20 (1996) 247–260.
- [24] J.C. Butcher, On Runge–Kutta methods of high order, *J. Aust. Math. Soc.* 4 (1964) 179–194.
- [25] J.C. Butcher, Coefficients for the study of the Runge–Kutta integration processes, *J. Aust. Math. Soc.* 3 (1963) 185–201.
- [26] J.C. Butcher, *Numerical Methods for Ordinary Differential Equations*, John Wiley & Sons, New York, 2003.
- [27] E. Fehlberg, *Classical Fifth, Sixth, Seventh and Eight Order Runge–Kutta Formulas with Stepsize Control*, NASA TR R-287, 1968.
- [28] J.R. Cash, A.H. Karp, A variable order Runge–Kutta method for initial value problems with rapidly varying right-hand sides, *ACM Trans. Math. Softw.* 16 (1990) 201–222.
- [29] J.H. Verner, Some Runge–Kutta formula pairs, *SIAM J. Numer. Anal.* 28 (1991) 496–511.
- [30] T. Feagin, A tenth-order Runge–Kutta method with error estimate, in: *Proceedings of the IAENG Conf. on Scientific Computing*, Hong Kong, 2007.
- [31] A.A. Kosti, Z.A. Anastassi, T.E. Simos, An optimized explicit Runge–Kutta method with increased phase-lag order for the numerical solution of the Schrödinger equation and related problems, *J. Math. Chem.* 47 (2010) 315–330.
- [32] T.E. Simos (Ed.), *Recent Advances in Computational and Applied Mathematics*, Springer Science+Business Media B.V., 2011.
- [33] A. Iserles, *A First Course in the Numerical Analysis of Differential Equations*, Cambridge Univ. Press, New York, 2009.
- [34] F.R. Moulton, *New Methods in Exterior Ballistics*, University of Chicago Press, Chicago, 1926.
- [35] P. Kralchevsky, R. Miller, F. Ravera (Eds.), *Colloid and Interface Chemistry for Nanotechnology*, CRC, Press, Boca Raton, FL, 2014.
- [36] R. Finn, *Equilibrium Capillary Surfaces*, Springer, New York, 2011.
- [37] S. Hartland, R. Hartley, *Axisymmetric Fluid–Liquid Interfaces*, Elsevier, Amsterdam, 1976.
- [38] H.J. Stetter, *Analysis of Discretization Methods for Ordinary Differential Equations*, Springer Verlag, New York, 1973.
- [39] V.A. Novikov, E.A. Novikov, Stability control of explicit one-step integration methods for ODE, *Dokl. Akad. Nauk SSSR* 277 (1984) 1058–1062 (in Russian).
- [40] E. Pitts, The stability of pendant liquid drops. Part 2. Axial symmetry, *J. Fluid Mech.* 63 (1974) 487–508.
- [41] E. Pitts, The stability of a drop hanging from a tube, *J. Inst. Math. Appl.* 17 (1976) 387–397.